# Characterization of Space-Time Focusing in Time-Reversed Random Fields

Claude Oestges, Arnold D. Kim, George Papanicolaou, and Arogyaswami J. Paulraj, *Fellow, IEEE*

***Abstract*—This paper proposes various metrics to characterize space-time focusing resulting from application of time reversal techniques in richly scattering media. The concept and goals of time reversal are presented. Pertinent metrics describing both the time and space focusing effects are outlined. Two examples based on a model of discrete and continuous scattering media are used to illustrate how the proposed metrics vary as a function of various system and channel parameters, such as the bandwidth, delay and angle spreads, number of antennas, etc.**

***Index Terms*—Random media, space-time focusing, time reversal.**

## I. Introduction

IN A TIME reversal (TR) experiment, a transducer captures the response received from an impulsive point source, and re-emits the time reversed version of this response into the propagation medium. For nondissipative media the emitted signal back-propagates and focuses in both space and time at the original impulsive source [1]–[3]. For richly scattering media, this space-time compression can be very strong. This basic principle is well known in acoustics and has lead to remarkable applications in underwater sound [4]–[12] and ultrasound [13]–[15].

The extension of TR techniques to radio electromagnetic propagation for wireless communications has yet to be precisely investigated. However, the idea of exploiting scattering is not new [16], [17]. Furthermore, there has been recently a tremendous activity in exploiting the richness of the scattering medium in space-time communications by using multiple antennas at both transmit and receive ends (i.e., multiple-input/multiple-output systems-MIMO) [18]. Nevertheless, current communication systems still rely on a fairly small communication bandwidth times channel delay-spread product $B \times \tau_{\mathrm{RMS}}$. By using a large $B \times \tau_{\mathrm{RMS}}$, it is believed that the transmitter can use an additional leverage of TR techniques to offer power gain and diversity gain together with space-time focusing. More precisely, TR techniques could be used to:

- *Reduce interference/intercept probability in view of secure communications.* By selectively focusing the energy in both space and time at a target point, TR ensures that intercept receivers will have difficulty detecting or decoding the intended signal. Similarly, the co-channel interference can be strongly reduced in cellular networks.
- *Shorten the temporal channel response.* The use of TR can dramatically lower the effective number of significant taps at the receiver, and lead to lower receiver complexity.

The goal of the paper is dual. First, characteristic metrics describing space-time focusing are presented in the context of time-reversed signals in wireless communications. They are estimated for two simplified models of random fields: a geometry-based stochastic channel model and a random-medium waveguide. Then we analyze the impact of system and channel parameters on the focusing by investigating the variation of the various metrics as a function of the channel properties (delay and angle spreads) and the system parameters (bandwidth, number of antennas, data rate, etc.). Both models are finally compared.

## II. Time-Reversed Random Fields

### A. Channel Impulse Response

Consider a transmission between transmit point $\mathbf{P}$ and receive point $\mathbf{Q}$. The channel impulse response (CIR) is denoted as $h_B(\tau, \mathbf{P} \rightarrow \mathbf{Q})$, where $B$ is the bandwidth of the transmitted pulse. It is important to note that

- the symmetry properties of usual transmission channels imply that $h_B(\tau, \mathbf{P} \rightarrow \mathbf{Q}) = h_B(\tau, \mathbf{Q} \rightarrow \mathbf{P})$;
- the CIR depends on the bandwidth of the transmitted pulse.

The so-called CIR is actually the convolution of the infinite-bandwidth physical channel response and the filter impulse response. In this paper, the filter is implemented as a Nyquist filter with given roll-off factor. By default, the roll-off is taken as equal to zero, so the default filter is a rectangular window in the frequency domain.

Depending on the scattering channel and the bandwidth, the CIR results in a temporal spreading of the initial pulse. Scatterers indeed create multipath mechanisms which, in turn, cause echoes to arrive at the receiver with different delays. However, the resolvability of the different delays depends upon the ratio of the inverse of the bandwidth to the physical channel spread (i.e., the interval between successive delays). The smaller $1/B$

Manuscript received January 20, 2004; revised March 26, 2004. The work of C. Oestges was supported by a grant from the Belgian NSF – Fonds National de la Recherche Scientifique (FNRS). The work of A. D. Kim and G. Papanicolaou was supported in part by Grant AFOSR: F49620-01-1-0465 and in part by Grant ONR: N00014-02-1-0088. The work of A. J. Paulraj was supported in part by NSF Contracts CCR-0241921, 0241919, ONR Contracts N00014-03-1-0766, N00014-03-1-0906, and in part by Intel Corporation.

C. Oestges is with the Belgian NSF – Fonds National de la Recherche Scientifique (FNRS), Microwave Laboratory, Université catholique de Louvain, 1348 Louvain-la-Neuve, Belgium (e-mail: oestges@emic.ucl.ac.be).

A. D. Kim was with the Department of Mathematics, Stanford University, Stanford, CA 94305-2125 USA. He is now with the School of Natural Sciences, University of California, Merced, CA 95344 2039 USA.

G. Papanicolaou is with the Department of Mathematics, Stanford University, Stanford, CA 94305-2125 USA (e-mail: papanico@math.stanford.edu).

A. J. Paulraj is a Professor at the Information Systems Laboratory, Stanford University, Stanford, CA 94305 USA (e-mail: apaulraj@stanford.edu).

Digital Object Identifier 10.1109/TAP.2004.836399

is relative to the channel delay spread, the larger is the number of resolved paths.

### B. Time-Reversal

*1) Time Domain Relationships:* Using the above formalism, the received signal at any point $\mathbf{R}$ for a Nyquist pulse emitted from $\mathbf{R}_0$ is $h_B(\tau, \mathbf{R}_0 \to \mathbf{R})$. At a particular point $\mathbf{T}$, which we define as the transponder, $h_B(\tau, \mathbf{R}_0 \to \mathbf{T})$ is captured. If the transponder sends back the time reversed version of the captured signal, i.e., $h_B(-\tau, \mathbf{R}_0 \to \mathbf{T})$, then at any point $\mathbf{R}$, the received signal can be expressed as

$$s_B(\tau, \mathbf{R}) = h_B(\tau, \mathbf{T} \to \mathbf{R}) \star h_B^*(-\tau, \mathbf{R}_0 \to \mathbf{T}) \quad (1)$$

where $\star$ denotes the convolution product and the superscript $*$ stands for complex conjugation. Note that (1) assumes a perfect estimation of $h_B(\tau, \mathbf{R}_0 \to \mathbf{T})$. In practical settings, noise and interference considerations will cause this estimation to be biased. We shall not cover the impact of imperfect channel estimation in this paper.

From now on, we define the point $\mathbf{R} = \mathbf{R}_0$ as the focal or target point. Based on (1) and on the symmetry properties mentioned above, the signal received at $\mathbf{R}_0$ is

$$s_B(\tau, \mathbf{R}_0) = h_B(\tau, \mathbf{R}_0 \to \mathbf{T}) \star h_B^*(-\tau, \mathbf{R}_0 \to \mathbf{T}). \quad (2)$$

As a consequence of (2), the time-reversal operation causes the received signal at $\mathbf{R}_0$ to be focused in both time and space through constructive interference, meaning that all multipath signals add coherently at $\mathbf{R}_0$, and incoherently elsewhere.

*2) Frequency Domain Relationships:* Models usually compute the channel transfer function $H_B(\omega, \mathbf{R}_0 \to \mathbf{T})$ over the system bandwidth (where $\omega$ is the angular frequency). It is the Fourier transform of $h_B(\tau, \mathbf{R}_0 \to \mathbf{T})$. Relationships (1) and (2) are easily written in the frequency domain, since the time-reversal operation corresponds to a complex conjugation in frequency

$$S_B(\omega, \mathbf{R}_0) = H_B(\omega, \mathbf{T} \to \mathbf{R}_0) H_B^*(\omega, \mathbf{R}_0 \to \mathbf{T}). \quad (3)$$

According to (3), the time-reversal operation is equivalent to a perfect channel matching.

We shall illustrate the characterization of $s_B(\tau, \mathbf{R})$, i.e., the quality of space-time focusing in two different space-time random fields. The first simulated random field corresponds to a typical wireless radio channel at 2.5 GHz. The second one is a continuous heterogeneous medium consisting of a filled waveguide also operating at 2.5 GHz.

## III. Modeling of Scattered Space-Time Fields

### A. Ray-Based Approach in Discrete Scattering Media: Geometry-Based Stochastic Model

For discrete scattering media, the channel can be represented by a number of effective scatterers randomly distributed in space. A ray-based approach can then be used to describe the channel as a sum of so-called scattered or reflected contributions. In the following, the statitical distribution of scatterers is based on the well-known one-ring model [19].

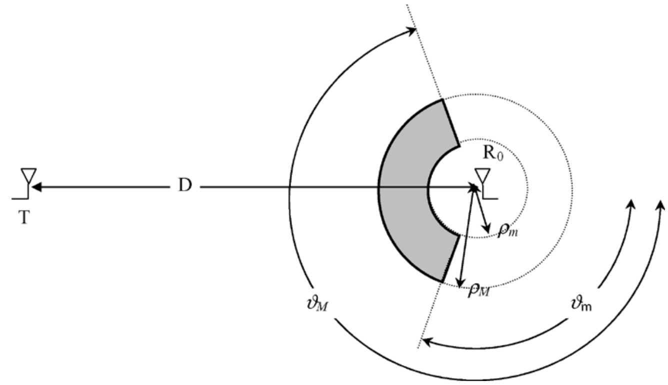


Fig. 1. Geometrical representation of the propagation model.

*1) Single-Bounce Model:* We first consider that only single scattering occurs. We assume that the scatterers are uniformly distributed inside an annular region surrounding the target point, as illustrated in Fig. 1. This region is specified by a minimal radius $\rho_m$ and a maximal radius $\rho_M$. The angle-spread of the channel (as seen from the target point) is fixed by limiting the aperture of the annular region to a given portion, i.e., specifying minimum and maximum angles, $\vartheta_m$ and $\vartheta_M$ (see Fig. 1). In this paper, we refer to $\Delta\vartheta = \vartheta_M - \vartheta_m$ as the scattering angle-spread or simply the angle-spread.

We further simplify the channel description by choosing $\rho_M = 2\rho_m$ and $\rho_M \ll D$, with $D$ denoting the distance between the transmit and target points. Hence, the RMS delay spread of the physical channel (over an infinite bandwidth) is well approximated for an omnidirectional distribution of scatterers ($\Delta\vartheta = 2\pi$) by

$$\tau_{\mathrm{RMS}} \approx \frac{\sqrt{5}\rho_m}{2c} \quad (4)$$

with $c = 3 \times 10^8$ m/s is the speed of light. For a limited angle spread, we assume that $\vartheta_m = \pi - \Delta\vartheta/2$ and $\vartheta_M = \pi + \Delta\vartheta/2$. In that case, the delay-spread can be written as

$$\tau_{\mathrm{RMS}} \approx \frac{\sqrt{5}\rho_m}{2c} \sqrt{\frac{\Delta\vartheta + \sin\Delta\vartheta}{2\pi}}. \quad (5)$$

The channel transfer function is easily estimated by means of a ray-tracing approach that yields

$$\begin{aligned} &H_B(\omega, \mathbf{R}_0 \to \mathbf{T}) \\ &= \sum_{l=1}^{N} G(\omega, \mathbf{R}_0 \to \mathbf{S}_l) \Gamma_l \times \left[ \frac{d_{\mathbf{R}_0\mathbf{S}_l} d_{\mathbf{S}_l\mathbf{T}}}{d_{\mathbf{R}_0\mathbf{S}_l} + d_{\mathbf{S}_l\mathbf{T}}} \right]^{\gamma/2} G(\omega, \mathbf{S}_l \to \mathbf{T}) \quad (6) \\ &= \sum_{l=1}^{N} \Gamma_l \frac{\exp\left[-j\omega(d_{\mathbf{R}_0\mathbf{S}_l} + d_{\mathbf{S}_l\mathbf{T}})\right]}{\left[d_{\mathbf{R}_0\mathbf{S}_l} + d_{\mathbf{S}_l\mathbf{T}}\right]^{\gamma/2}}. \quad (7) \end{aligned}$$

The quantities in (6) and (7) are

- $\omega = 2\pi/\lambda$, the angular frequency ($\lambda$ denoting the wavelength);
- $G(\omega, \mathbf{P} \to \mathbf{Q}) = \exp(-j\omega d_{\mathbf{PQ}})/(d_{\mathbf{PQ}})^{\gamma/2}$, the spreading function for a transmission from $\mathbf{P}$ to $\mathbf{Q}$, with $\gamma$ denoting the effective path-loss exponent ($\gamma \geq 2$) and $d_{\mathbf{PQ}}$ denoting the distance between $\mathbf{P}$ and $\mathbf{Q}$;

- $\Gamma_l$, the scattering coefficient of the $l$th scatterer, whose magnitude is comprised between 0 and 1; in this paper, it is considered to be a complex Gaussian variable, with given standard deviation;
- $[d_{\mathbf{R}_0\mathbf{S}_l}d_{\mathbf{S}_l\mathbf{T}}/(d_{\mathbf{R}_0\mathbf{S}_l}+d_{\mathbf{S}_l\mathbf{T}})]^{\gamma/2}$ is the usual spreading factor for reflection [20], ensuring that the transfer function is inversely proportional to the total distance, as outlined by (7); multiplying this reflection spreading factor by $\Gamma_l$ yields the so-called scattering cross-section.

Single-bounce models are not sensitive to the order of magnitude of $\Gamma$ and $\gamma$ since they are only responsible for a proportionality factor. This is not the case for multiple-bounce models in which the average loss per interaction, related to the scattering cross-section and the path-loss, is a critical parameter.

*2) Multiple-Bounce Model:* The previous model can be extended in order to consider multiple bounce interactions. In other words, the transmitted waves are scattered from one to a certain number of times before reaching the receiver. The calculation of the transmission channel can be written as a sum of $N$ scattered contributions

$$H_B(\omega,\mathbf{R}_0\rightarrow\mathbf{T})=\sum_{l=1}^{N}C_l\eta_l G(\omega,\mathbf{S}_l\rightarrow\mathbf{T}) \tag{8}$$

where

- $G(\omega,\mathbf{S}_l\rightarrow\mathbf{T})$ is the spreading function for a transmission from the $l$th scatterer to the target point $\mathbf{T}$;
- $\eta_l$ is the scattering cross-section of the $l$th scatterer, proportional to the scattering coefficient $\Gamma_l$ [21];
- $C_l$ is the $l$th element of vector $\mathbf{C}$, which is the solution of a $N$-order linear system given by

$$\mathbf{C}=\mathbf{A}^{-1}\cdot\mathbf{C}_0 \tag{9}$$

with

- $C_{0l}=G(\omega,\mathbf{R}_0\rightarrow\mathbf{S}_l)$ is the channel between the target point and the location of each scatterer;
- $\mathbf{A}$ is the system matrix accounting for the transmission between each pair of scatterers

$$A_{kl}=\begin{cases}\Gamma_k G(\omega,\mathbf{S}_k\rightarrow\mathbf{S}_l), & k\neq l,\\ 1, & k=l.\end{cases} \tag{10}$$

As already mentioned, the model is then highly sensitive to the average loss per interaction, i.e., to the product $|\eta_k G(\omega,\mathbf{S}_k\rightarrow\mathbf{S}_l)|$. On one hand, if the latter is very small, then the delay-spread of the channel tends to be infinite, which is unrealistic. On the other hand, if the loss per interaction is very large, the impact of high-order scattered contributions becomes small, and the received field is very similar to the first-order field. A reasonable assumption is that contributions up to the third order can be significant. The average loss per interaction should then be chosen accordingly. One could question the usefulness of the matrix formulation as compared to a full third-order ray-tracing computation. The reasons for preferring the matrix formulation are two-fold:

- the problem of the average loss per interaction is not related to the matrix formulation, but to any multiple-bounce model;
- the computation time of a full ray-tracing is prohibitive as compared to the fast matrix algorithm.

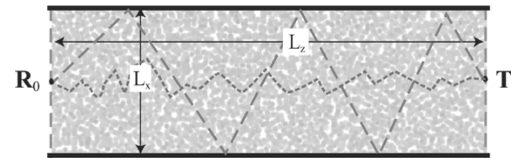


Fig. 2. Sketch of the random waveguide model with two rays from the source at $\mathbf{R}_0$ propagating to the transponder at $\mathbf{T}$ each undergoing one of the two mechanisms for multipathing: reflection from walls and scattering by inhomogeneities.

### *B. Phase Screen Method in Continuous Scattering Media: Waveguide Model*

We investigate guided wave propagation in two dimensions. The interior of a periodic waveguide is a weakly scattering medium. Signals propagating through this waveguide experience significant multipathing yielding a large delay-spread. This model is an interesting theoretical counterpart to the geometry-based model, in the sense that scattering is now partly continuous. Moreover, this model can seen as an approximation of propagation through hallways inside buildings or urban canyons.

Here, multipathing is due to two different mechanisms: reflections from the waveguide walls and scattering by the inhomogeneities. Fig. 2, shows a sketch of this waveguide and two rays propagating from the source at $\mathbf{R}_0$ to the transponder $\mathbf{T}$. One ray reaches $\mathbf{T}$ after several reflections from the waveguide walls. The other one reaches $\mathbf{T}$ by multiple scattering events due to the inhomogeneities inside. In fact, the source at $\mathbf{R}_0$ produces an entire angular spectrum of rays over the bandwidth. Furthermore, the signals reaching $\mathbf{T}$ undergo a mixture of these two multipathing effects.

The waveguide width is $L_x$ and the distance along the waveguide between $\mathbf{R}_0$ and $\mathbf{T}$ is $L_z$. We also assume that the initial transmitted signal at $\mathbf{R}_0$ can be given a limited angular aperture $\vartheta$. For the sake of simplicity, the mean refractive index is chosen as unity (note that changing this value only affects the overall phase of the computation). The fluctuation is an isotropic, Gaussian correlated random function of space. The random fluctuation has RMS height $h_{\mathrm{RMS}}$ and correlation length $\ell$.

To compute the random space-time field, we place equi-spaced phase screens inside the waveguide separated in distance by $\ell$. Simulating propagation along the waveguide involves combining a sequence of steps from one screen to the next. Each step involves propagation through an "empty" waveguide followed by a random phase correction.

We now describe a single step in the phase screen method. Let $z_{n-1}$, $z_n$ and $z_{n+1}$ denote locations of three consecutive phase screens. We assume that the channel transfer function $H_B(\omega,z_{n-1}\rightarrow z_n)$ from $z_{n-1}$ to $z_n$ is known. Because the waveguide is periodic, we express it as a Fourier series

$$H_B(\omega,z_{n-1}\rightarrow z_n)=\sum_{m=-\infty}^{\infty}a_m(\omega,z_n)e^{j2\pi mx/L_x}. \tag{11}$$

The channel transfer function for $z_n$ to $z_{n+1}$ is then given by

$$H_B(\omega, z_n \to z_{n+1}) = e^{jk\tilde{\mu}(x)\delta z/2} \times \left[ \sum_{m=-\infty}^{\infty} T_m(\omega, \delta z) a_m(\omega, z_n) e^{j2\pi mx/L_x} \right] \quad (12)$$

with $\delta z = z_{n+1} - z_n$ and $k = 2\pi/\lambda$ the wavenumber. The forward propagation operator $T_m(\omega, \delta z)$ is defined as

$$T_m(\omega, \delta z) = \exp\left[ jk\sqrt{1 - \left(\frac{2\pi m}{(kL_x)}\right)^2}\,\delta z \right]. \quad (13)$$

The random phase correction $\tilde{\mu}(x)$ is a path-integral of the fluctuation $\mu(x,z) = 1 - n^2(x,z)$ between the screens $z_n$ and $z_{n+1}$ with $n(x,z)$ denoting the index of refraction inside the waveguide.

To limit the angular aperture for the initial transmit at $\mathbf{R}_0$, we filter the Fourier modes before updating the field to the next phase screen. Let $z_0$ denote the phase screen containing $\mathbf{R}_0$ and $\Psi(\omega, z_0, x)$ denote the initial transmit signal which we express as the Fourier series

$$\Psi(\omega, z_0, x) = \sum_{m=-\infty}^{\infty} \psi_m(\omega) e^{j2\pi mx/L_x}. \quad (14)$$

From (13), we determine that propagating modes are those for which

$$|m| < \frac{kL_x}{2\pi}. \quad (15)$$

All others are evanescent. For a propagating mode, the propagation angle is determined from $\sin\vartheta_m = 2\pi m/(kL_x)$. The largest value of $m$ such that (15) holds gives the largest propagation angle $\vartheta_{\max}$. To set the angular aperture of the initial transmit $\vartheta$, we restrict the summation in (15) to modes $m$ such that $\vartheta_m \leq \vartheta$.

## IV. Characteristic Parameters of Space-Time Focusing

### A. Space-Time Functions

The space-time received signal $s_B(\tau, \mathbf{R})$ is converted into characteristic metrics by considering the following.

- the energy of $s_B(\tau, \mathbf{R})$ at any point $\mathbf{R}$ in space, at a given time $\tau_0$, i.e.

$$\eta_D(\mathbf{R}) = |s_B(\tau_0, \mathbf{R})|^2 \quad (16)$$

  with $\tau_0$ such that $|s_B(\tau_0, \mathbf{R}_0)| = \max_\tau\{|s_B(\tau, \mathbf{R}_0)|\}$.
- the RMS delay spread of $s_B(\tau, \mathbf{R})$ (on a realization basis)

$$\Delta\tau(\mathbf{R}) = \sqrt{\frac{\int (\tau - \tau_m)^2 |s_B(\tau, \mathbf{R})|^2 d\tau}{\int |s_B(\tau, \mathbf{R})|^2 d\tau}} \quad (17)$$

  where $\tau_m$ is the average delay defined as

$$\tau_m(\mathbf{R}) = \frac{\int \tau |s_B(\tau, \mathbf{R})|^2 d\tau}{\int |s_B(\tau, \mathbf{R})|^2 d\tau}.$$

Note that the above definitions assume that the received space-time signal is sampled correctly in time so that the maximal amplitude can be captured. An alternative definition of $\eta(\mathbf{R})$ would be to consider the peak energy, independently from the time delay

$$\eta_M(\mathbf{R}) = \left[\max_\tau\{|s_B(\tau, \mathbf{R})|\}\right]^2. \quad (18)$$

Both $\eta_D(\mathbf{R})$ or $\eta_M(\mathbf{R})$ and $\Delta\tau(\mathbf{R})$ are random spatial functions, which can be characterized by their first-order moments.

### B. Spatial Focusing

The spatial focusing around the focal point is described by two parameters.

The asymptotic space-focusing gain (SFG) is given by

$$p_D = \lim_{|\mathbf{R}-\mathbf{R}_0|\to\infty} \frac{\eta_D(\mathbf{R}_0)}{\eta_D(\mathbf{R})}. \quad (19)$$

It is the ratio between the energy at $\mathbf{R}_0$ to the energy at long distance from $\mathbf{R}_0$. A large value of this ratio indicates better space focusing. Note that $p_M$ is defined similarly with respect to $\eta_M(\mathbf{R})$, and that $p_D$ could be defined at different time delays, i.e., other than $\tau_0$.

The 3-dB contour of the energy function $\eta_D(\mathbf{R})$ or $\eta_M(\mathbf{R})$ can be considered as the focusing region. It is described by the distance in both range and cross-range for which $\eta_D(\mathbf{R})$ or $\eta_M(\mathbf{R})$ remains within 3 dB below the energy at $\mathbf{R}_0$. The characteristic parameters $G_a$ and $G_x$ are therefore defined such that

$$\frac{\eta_D(\mathbf{R}_0 + G_a\mathbf{u}_a)}{\eta_D(\mathbf{R}_0)} = 0.5 \quad (20a)$$

$$\frac{\eta_D(\mathbf{R}_0 + G_x\mathbf{u}_x)}{\eta_D(\mathbf{R}_0)} = 0.5 \quad (20b)$$

where $\mathbf{u}_a$ and $\mathbf{u}_x$ are unit vectors, respectively in the range and cross-range directions. Note that the definition of $G_a$ and $G_x$ may similarly rely on $\eta_M(\mathbf{R})$. However, our simulation results show that $G_a$ and $G_x$ appear to be independent of the definition of the energy function.

### C. Time Focusing

The time focusing at the focal point is described by the RMS delay spread of $s_B(\tau, \mathbf{R})$ at $\mathbf{R} = \mathbf{R}_0$, denoted as $\Delta\tau_0 = \Delta\tau(\mathbf{R}_0)$. Note that this delay-spread is expressed in (17), and accounts for the pulse width.

Finally, a time focusing gain (TFG) is also suitably defined by the relative increase of RMS delay spread $\Delta\tau(\mathbf{R})$ at any point $\mathbf{R}$ compared to $\mathbf{R}_0$. The parameter is denoted as

$$\sigma(\mathbf{R}) = \frac{\Delta\tau(\mathbf{R}) - \Delta\tau_0}{\Delta\tau_0}. \quad (21)$$

The asymptotic TFG is given by $\lim_{|\mathbf{R}-\mathbf{R}_0|\to\infty} \sigma(\mathbf{R})$. A larger TFG indicates better temporal focusing in the sense that the time compression at the focal point with respect to any point away from the focal point becomes larger.

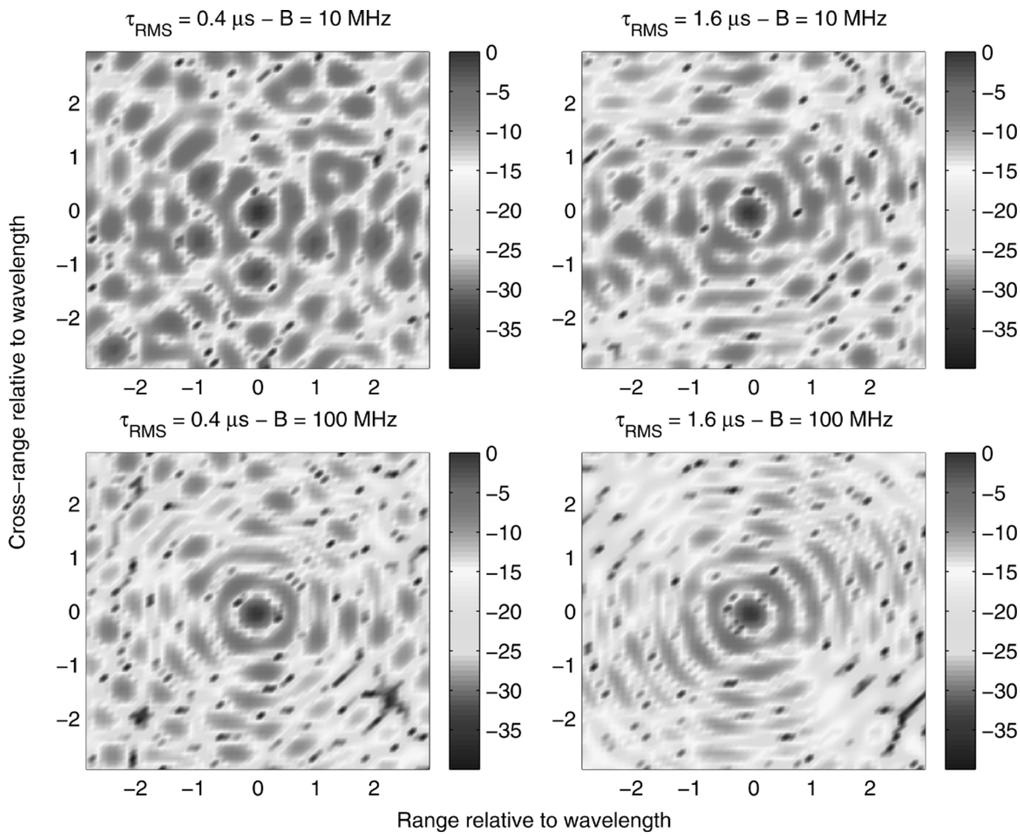


Fig. 3. Typical one-shot realizations of time reversed random fields (the energy function is expressed in decibels).

The metrics descrived above are random variables or functions per channel realization. Hence, they are characterized by their mean and variance taken over all realizations.

## V. Characterization of Focusing for Time Reversed Fields

We characterize time reversed fields computed from the two different models described in Section III. For each case the above metrics are computed, and relationships between these metrics and several parameters are pointed out.

### *A. Geometry-Based Stochastic Model*

In the context of the proposed geometry-based stochastic (GS) model, we have carried out simulations using the following parameters:

- the central frequency is 2.5 GHz;
- the transponder is separated from the target point by a distance of $10^4$ wavelengths, i.e., 1.2 km;
- when the delay spread is not used as a variable or explicitly assigned a specific value, it is fixed at $0.8\mu$s (i.e., $\rho_m = 1800\lambda$);
- different angle spreads, ranging from $\pi/3$ to $2\pi$;
- the effective path-loss exponent is set to 2, and the scattering coefficient is assumed to be complex Gaussian distributed with standard deviation of 0.25.

Fig. 3, shows snapshots of $\eta_D(\mathbf{R})$ (the target point is in the center of the figure), for two bandwidths: 50 and 100 MHz, two channel delay spreads and omnidirectional angular spreading of the scatterers (only single scattering is considered in a first step).

The impact of both the bandwidth and the channel delay-spread is clearly visible (the scales are kept constant from graph to graph). For the smallest $B \times \tau_{\mathrm{RMS}}$ product, some areas receive the same level of energy as the target point. For the largest $B\times\tau_{\mathrm{RMS}}$ product, the space focusing gain is about 15 to 20 dB. Also, it seems that the instantaneous energy function is oscillating as a function of the distance to the focal point.

*1) Omnidirectional Scattering Results:* For omnidirectional single scattering around the target point, Fig. 3 shows that the space-time focusing is improved when both the bandwidth and the delay-spread are increased. Figs. 4 and 5, show $E\{\eta_D(\mathbf{R})/\eta_D(\mathbf{R}_0)\}$ and $E\{\Delta\tau(\mathbf{R})\}$ as a function of the system bandwidth. The channel delay spread is set to 0.8 $\mu$s for these simulations.

The simulated dependencies have been fitted by the following empirical formulas:

$$E\{p_D\} = \bar{p}_D = 5.9\tau_{\mathrm{RMS}}^{0.29}B^{0.35} \tag{22}$$

$$E\{p_M\} = \bar{p}_M = 2.2\tau_{\mathrm{RMS}}^{0.24}B^{0.52} \tag{23}$$

$$E\left\{\frac{\eta_D(\mathbf{R})}{\eta_D(\mathbf{R}_0)}\right\} \cong K_D + (1-K_D)\times\left|J_0\left(\frac{2\pi|\mathbf{R}-\mathbf{R}_0|}{\lambda}\right)\right|^{\alpha} \times \exp\left(-\frac{|\mathbf{R}-\mathbf{R}_0|}{3.2\lambda}\right) \tag{24}$$

with

$$\alpha = 2.6\exp\left(-\frac{\tau_{\mathrm{RMS}}}{1.23}\right) \tag{25}$$

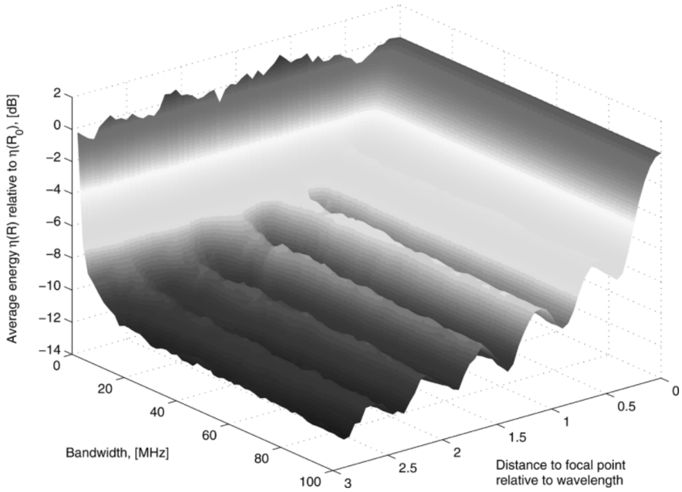


Fig. 4. Simulated energy function $E\{\eta_D(\mathbf{R})/\eta_D(\mathbf{R}_0)\}$ as a function of range and bandwidth.

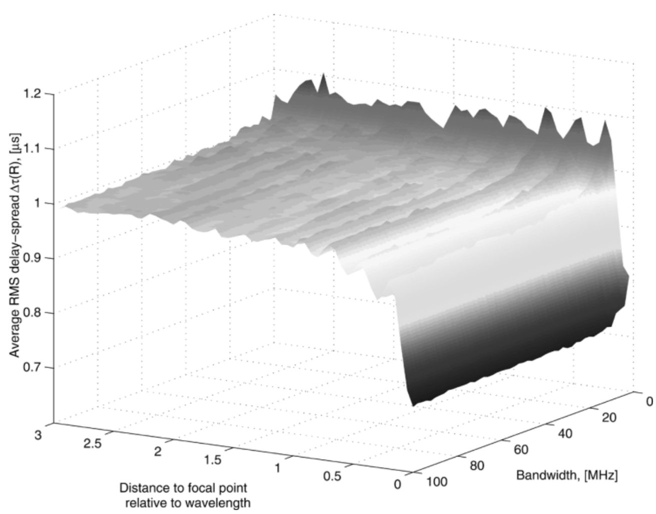


Fig. 5. Simulated RMS delay spread $E\{\Delta\tau(\mathbf{R})\}$ as a function of range and bandwidth.

and

$$K_D \propto \frac{1}{\bar{p}_D} \tag{26}$$

$$\frac{\bar{G}_a}{\lambda} = \frac{\bar{G}_x}{\lambda} = 0.41\tau_{\mathrm{RMS}}^{-0.01}B^{-0.02} \tag{27}$$

$$\overline{\Delta\tau}_0 = 0.083\tau_{\mathrm{RMS}}^{-1.25}B^{-1} + 0.93\tau_{\mathrm{RMS}}^{0.92} \tag{28}$$

$$E\{\sigma(\mathbf{R})\} \cong 0.37\left\{1 - \left|J_0\left(\frac{2\pi|\mathbf{R}-\mathbf{R}_0|}{\lambda}\right)\right|^{\beta} \times \exp\left(-\frac{|\mathbf{R}-\mathbf{R}_0|}{1.5\lambda}\right)\right\} \tag{29}$$

with $\beta = 1.3\exp(-\tau_{\mathrm{RMS}}/1.8)$. Here, the bandwidth $B$ is expressed in MHz, and the delay-spread $\tau_{\mathrm{RMS}}$ is expressed in $\mu$s.

The alternative energy ratio $E\{\eta_M(\mathbf{R})/\eta_M(\mathbf{R}_0)\}$ can be expressed in the same fashion as in (24).

- In (22), (27), and (28), exponents for $B$ and $\tau_{\mathrm{RMS}}$ are roughly similar as soon as both variables appear multiplied by each other. This observation implies that space-time focusing in general is related to the product $B \times \tau_{\mathrm{RMS}}$. So, we can affirm that the quality of space-time focusing is improved by increasing the product $B\times\tau_{\mathrm{RMS}}$. However, that assertion should be nuanced, since some terms in (28) and (29), as well as $\alpha$ and $\beta$ are only related to the channel delay-spread.
- When $B$ is sufficiently large ($> 10$), the space-focusing parameters depend upon $B \times \tau_{\mathrm{RMS}}$. This impact is significant regarding the asymptotic SFG. However, the dependence of the 3-dB contour width toward $B\times\tau_{\mathrm{RMS}}$ is much weaker. Both $G_a$ and $G_x$ are therefore mostly inversely proportional to the carrier frequency only. Note that for smaller bandwidths (for which (22) and (23) are not valid anymore), the average asymptotic SFG tends to unity.
- The average delay spread at the focal point $\overline{\Delta\tau}_0$ results from the additive combination of two terms: one roughly related to $B \times \tau_{\mathrm{RMS}}$, and the other one to $\tau_{\mathrm{RMS}}$ only. For large $B \times \tau_{\mathrm{RMS}}$, the variation of $\overline{\Delta\tau}_0$ with $B$ becomes weak, so $\overline{\Delta\tau}_0$ equal to the channel delay-spread. This is clearly visible on Fig. 5. At any other point $\mathbf{R}$ outside the focusing region, the average delay spread $E\{\Delta\tau(\mathbf{R})\}$ is an oscillating increasing exponential function of the distance from the focal point. It saturates at long distances.
- At any point $\mathbf{R}$, the time-focusing gain $E\{\sigma(\mathbf{R})\}$ is only related to the channel delay-spread. Furthermore, the asymptotic TFG (i.e., at long distance) is a constant value ($\sim 0.37$) independent from $B$ and $\tau_{\mathrm{RMS}}$, at least for sufficiently large $B \times \tau_{\mathrm{RMS}}$ ($> 10$).

*2) Impact of Reduced Angular Spread:* We also investigate how anglular spreading affects the quality of space-focusing. When the angle spread is decreased from $2\pi$ to smaller angles, the spatial focusing is degraded as expected.

- For $\Delta\vartheta > \pi/3$, the asymptotic SFG $\bar{p}_D$ decreases as $\Delta\vartheta$ decreases. It varies as $(\Delta\vartheta/2\pi)^{0.6}$ relatively to the simulated $\bar{p}_D$ with $\Delta\vartheta = 2\pi$.
- The 3-dB contours $\bar{G}_a$ and $\bar{G}_x$ are not identical anymore, and $\bar{G}_a \cong 4\bar{G}_x$ for $\Delta\vartheta \leq 3\pi/4$. They are decreased respectively by $\Delta\vartheta^{-1.3}$ and $\Delta\vartheta^{-1.2}$ relatively from their previous values (i.e., when $\Delta\vartheta$ was equal to $2\pi$). For $\Delta\vartheta > 3\pi/4$, the ratio $\bar{G}_a(\Delta\vartheta)/\bar{G}_a(\Delta\vartheta = 2\pi)$ continues to decrease following a $\Delta\vartheta^{-1.3}$ law while $\bar{G}_x(\Delta\vartheta)/\bar{G}_x(\Delta\vartheta = 2\pi)$ remains constant. Hence, $\bar{G}_a = \bar{G}_x$ for $\Delta\vartheta = 2\pi$.

New empirical expressions can therefore be derived easily that take into account that the channel delay spread $\tau_{\mathrm{RMS}}$ is also modified when reducing the angle spread, as highlighted by (4) and (5)

$$\bar{p}_D = 5.9\tau_{\mathrm{RMS}}^{0.29}B^{0.35}\left(\frac{\Delta\vartheta}{2\pi}\right)^{0.6}\nu^{-0.2} \tag{30}$$

with $\nu = (\Delta\vartheta + \sin\Delta\vartheta)/(2\pi)$

$$\frac{\bar{G}_a}{\lambda} = 0.41\tau_{\mathrm{RMS}}^{-0.01}B^{-0.02}\left(\frac{\Delta\vartheta}{2\pi}\right)^{-1.3}\nu^{0.005} \approx 0.41\left(\frac{\Delta\vartheta}{2\pi}\right)^{-1.3} \tag{31}$$

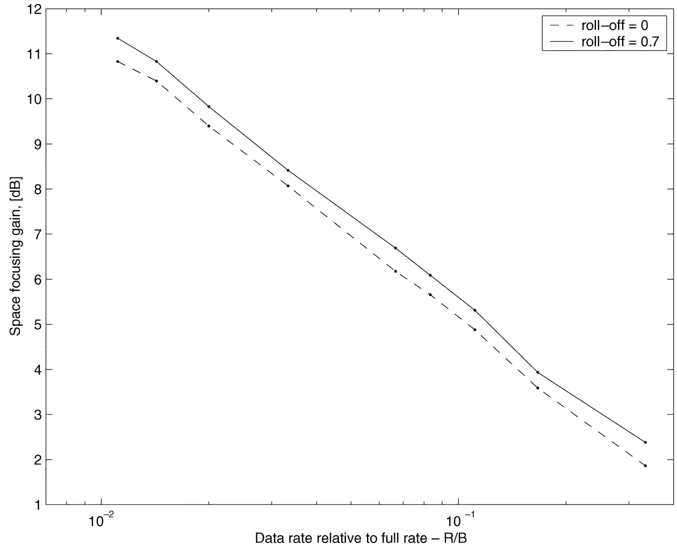


Fig. 6. Spatial focusing gain as a function of data rate and roll-off factor.

$$\frac{\bar{G}_x}{\lambda} = \begin{cases} 0.13\tau_{\mathrm{RMS}}^{-0.01}B^{-0.02}\left(\frac{\Delta\vartheta}{2\pi}\right)^{-1.2}\nu^{0.005}, & \frac{\pi}{3}\le\Delta\vartheta\le\frac{3\pi}{4} \\ 0.41\tau_{\mathrm{RMS}}^{-0.01}B^{-0.02}\nu^{0.005}, & \Delta\vartheta>\frac{3\pi}{4} \end{cases}$$
$$\approx \begin{cases} 0.13\left(\frac{\Delta\vartheta}{2\pi}\right)^{-1.2}, & \frac{\pi}{3}\le\Delta\vartheta\le\frac{3\pi}{4} \\ 0.41\left(\frac{\Delta\vartheta}{2\pi}\right)^{-1.3}, & \Delta\vartheta>\frac{3\pi}{4}. \end{cases} \quad (32)$$

*3) Benefits From Multiple Antennas:* The impact of using multiple antennas at the transmit point is analyzed in the following. At the transmit point, the terminal consists of $M_T$ antennas. Each antenna has a specific location around $\mathbf{T}$, denoted as $\mathbf{T}_u$. Hence, the focused signal is written as

$$s_B(\tau,\mathbf{R}_0) = \frac{1}{\sqrt{M_T}}\sum_{u=1}^{M_T} h_B(\tau,\mathbf{R}_0\to\mathbf{T}_u)\star h_B^*(-\tau,\mathbf{R}_0\to\mathbf{T}_u) \quad (33)$$

where the scaling factor $1/\sqrt{M_T}$ ensures that the total transmitted power is kept constant, irrespective of the number of antennas.

Increasing the number of antennas should increase the space-time focusing. Simulations actually show that $G_a$ and $G_x$ remain unaffected when the number of antennas is increased. Regarding the SFG, the benefit from multiple antennas is proportional to $M_T$. This corresponds to the well-known diversity results [18]. Indeed, considering a constant transmitted power, the peak energy at the focal point will grow as $M_T^2/M_T = M_T$, but will behave as $M_T/M_T = 1$ anywhere else outside the focusing region.

*4) Multiple Bounce Propagation Model:* We now consider the multiple bounce model. As mentioned previously, this model is sensitive to the path-loss exponent and the distribution of scattering cross-section. For an average loss per additional reflection of 12 dB, the impact of multiple reflections on the focusing is negligible. If the average loss per interaction is decreased by 4 dB, the impact, though not negligible, remains small. This is mostly because the large number of scatterers enables the time-reversed field to be highly focused with single-bounce interactions.

*5) Space-Time Focusing in Time-Reversed Transmissions:* So far, we have assumed that a single time-reversed pulse is sent from the transmitter to the target point. This section analyzes how space-time focusing is affected when sending a time-reversed signal. The latter consists of the convolution of the time-reversed pulse with a train of information bits.

Fig. 6 shows the SFG as a function of the relative data rate (i.e., the data rate relative to the pulse bandwidth) for two different Nyquist roll-off factors. The bandwidth is equal to 40 MHz and the channel RMS delay-spread to 0.8 $\mu$s. For these values the single-pulse SFG $\bar{p}_D \approx 13$ dB. It is clear from Fig. 6 that for the full rate the space focusing advantage is totally destroyed.

The limit to which the data rate can be increased without destroying focusing is related strongly to the coherence bandwidth of the channel transfer function. This coherence bandwidth gives the frequency difference at which phases become decorrelated and is inversely proportional to the delay spread. Encoding on frequency intervals smaller than the coherence bandwidth destroys spatial information contained in the channel transfer function resulting in poor focusing.

In fact, Fig. 6 shows that space focusing is slowly restored as this rate decreases. It is about 5 to 6 dB for a rate of $B/10$. For this high roll-off factor, the degradation is approximately 0.5 dB less than for the zero roll-off case. This is not surprising since higher roll-off factors yield lower side lobes.

Therefore, there is a tradeoff between the data rate and the spatial focusing effect that can be achieved in a wireless channel for a given bandwidth. This tradeoff is dictated by the coherence bandwidth of the channel transfer function. For the example given in Fig. 6, rates lower than $B/10$ are needed to maintain a sufficient level of focusing.

## *B. Waveguide Model*

Numerical simulations in the waveguide have been carried out using the following parameters:

- the central frequency is 2.5 GHz;
- the length $L_z$ is 100 m;
- the refractive index fluctuation has RMS height $h_{\mathrm{RMS}} = 0.05$ and correlation length $\ell = 1.0$ m;
- the waveguide width $L_x$ is either 12.8, 25.6, or 51.2 m;
- the source angle $\vartheta$ is either 25°, 45° or 65°;
- the bandwidth $B$ is between 10 and 100 MHz.

The focus point $\mathbf{R}_0$ is centered in the waveguide. We set $\mathbf{R}_0$ to be the origin for the $x-z$ coordinate system. The transponder is located 100 m down-range from $\mathbf{R}_0$. It is an array spanning $1\ \mathrm{m} \le x \le 2\ \mathrm{m}$. Note that the array center is deliberately slightly skewed from $x=0$ as to break any symmetry. Hence, any observed effect is by no means an artifact caused by symmetry. Note that our numerical results have shown that the space-time focusing is insensitive to the location of the transponder array as lons as there is sufficient multipathing in the channel.

Figs. 7 and 8, show $\eta_D(x,z_0)/\eta_D(x_0,z_0)$ and $\Delta\tau(x,z_0)$ respectively for a waveguide of width 25.6 m. Averages were computed for 500 realizations of the random refractive index. Results are shown for bandwidths of 10, 20, 40, 80, and 100 MHz.

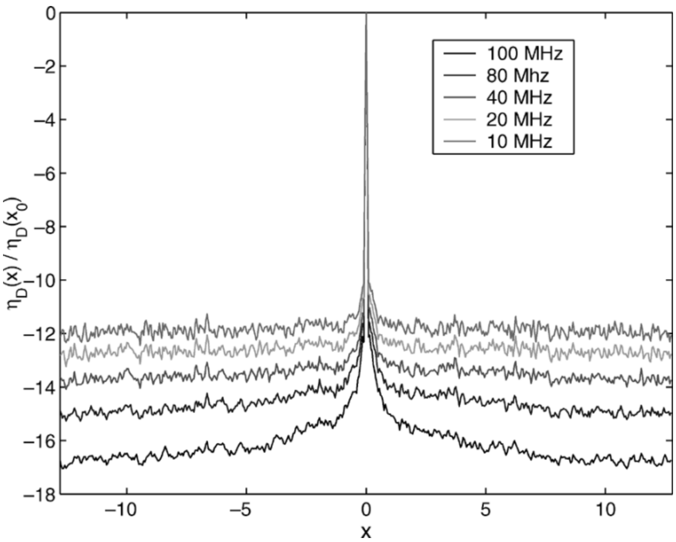


Fig. 7. Energy of $s_B(\tau_0, x)$ in a waveguide with width $L_x = 25.6$ m and $L_z = 100$ m averaged over 500 realizations of the random refractive index. The source is limited in angle by $\Delta\vartheta = 45°$ and in bandwidth by 100, 80, 40, 20, and 10 MHz.

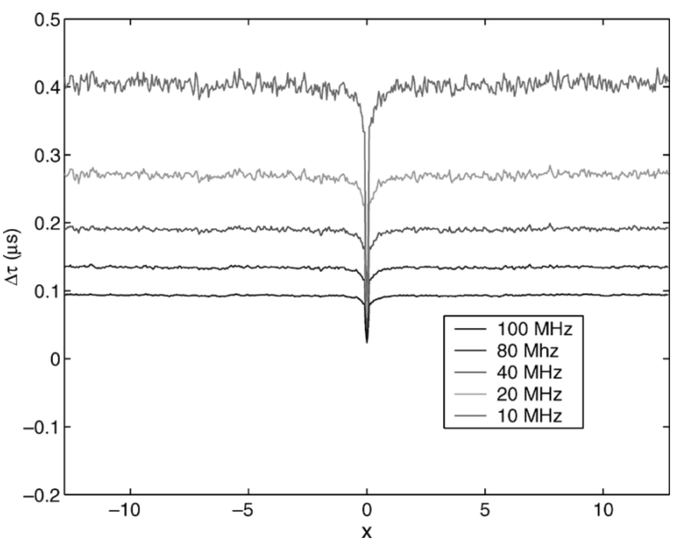


Fig. 8. RMS delay spread $\tau_{\mathrm{RMS}}$ averaged over 500 realizations of the random refractive index. All other parameters are the same as in Fig. 7.

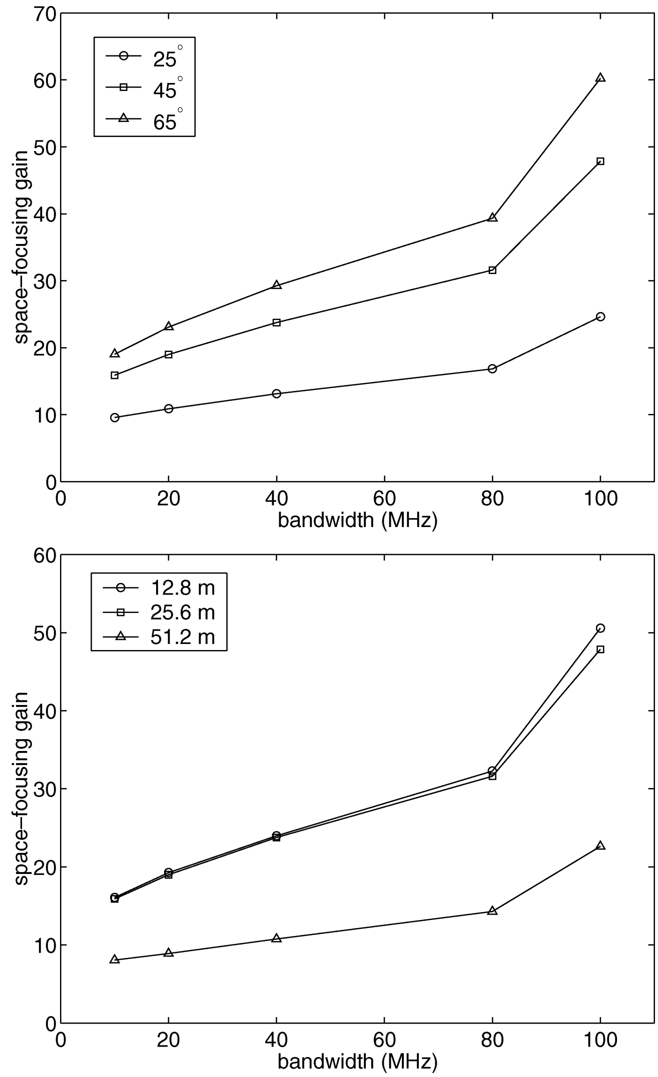


Fig. 9. Asymptotic space-focusing gain (SFG) as a function of bandwidth for different source angles (top) with waveguide width $L_x = 25.6$ m and different waveguide widths (bottom) with source angle $\Delta\vartheta = 45°$.

In Fig. 7, we observe that quality of spatial focus about $x_0 = 0$ is nearly the same over all bandwidths. However, the energy away from the refocus location decreases as the bandwidth increases. In particular, we observe a 5 dB difference between the 10 MHz and 100 MHz cases.

In Fig. 8, we observe the quality of temporal focus about $x_0 = 0$ where $\Delta\tau$ is smallest. Because a larger bandwidth yields a shorter pulse, $\Delta\tau$ is smaller for larger bandwidths. Nonetheless, we observe that these curves become smoother as the bandwidth increases. This phenomenon is due to the onset of statistical stability manifested from broad bandwidth signals [22].

To examine spatial focusing in greater detail, we show the space-focusing gain in Fig. 9. The top plot is for $L_x = 25.6$ m with different values of $\vartheta$. The bottom plot is for $\vartheta = 45°$ with different values of $L_x$. As we have already mentioned, adding bandwidth to the system reduces the energy away from the refocus location. Fig. 9 further demonstrates this since all curves show that SFG increases with bandwidth. The top plot in Fig. 9 shows that limiting $\vartheta$ reduces the SFG. The bottom plot shows that there is little difference between the $L_x = 12.8$ m and 25.6 m cases. However, the SFG for the $L_x = 51.2$ m case is much smaller than the other two. For a fixed $\vartheta$, widening the waveguide reduces the diversity of modes that propagate in the channel. This reduction, in turn, reduces the quality of focus in time reversal.

In addition, we show the 3-dB contour in cross-range $G_x$ in Fig. 10. Similar to Fig. 9, the top plot is for $L_x = 25.6$ m with different values of $\vartheta$ and the bottom plot is for $\vartheta = 45°$ with different values of $L_x$. Here, we observe that cross-range dependence of the 3-dB contour changes very little with respect to bandwidth. Because limiting the angular aperture of the source is a spatial low-pass filter yielding broader initial transmit sources, $G_x$ increases as $\vartheta$ decreases. For different waveguide widths, the 3-dB contour does not change significantly. It decreases slightly as the width increases because of added angular

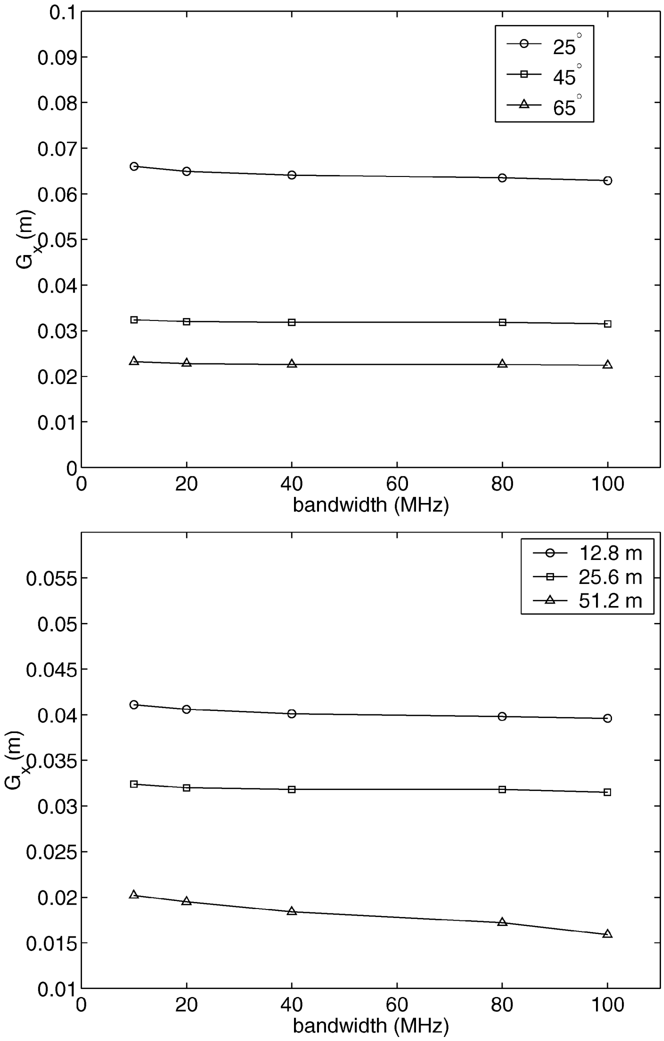


Fig. 10. 3-dB contour in cross-range $G_x$ as a function of bandwidth for different source angles (top) with waveguide width $L_x = 25.6$ m and different waveguide widths (bottom) with source angle $\Delta\vartheta = 45°$.

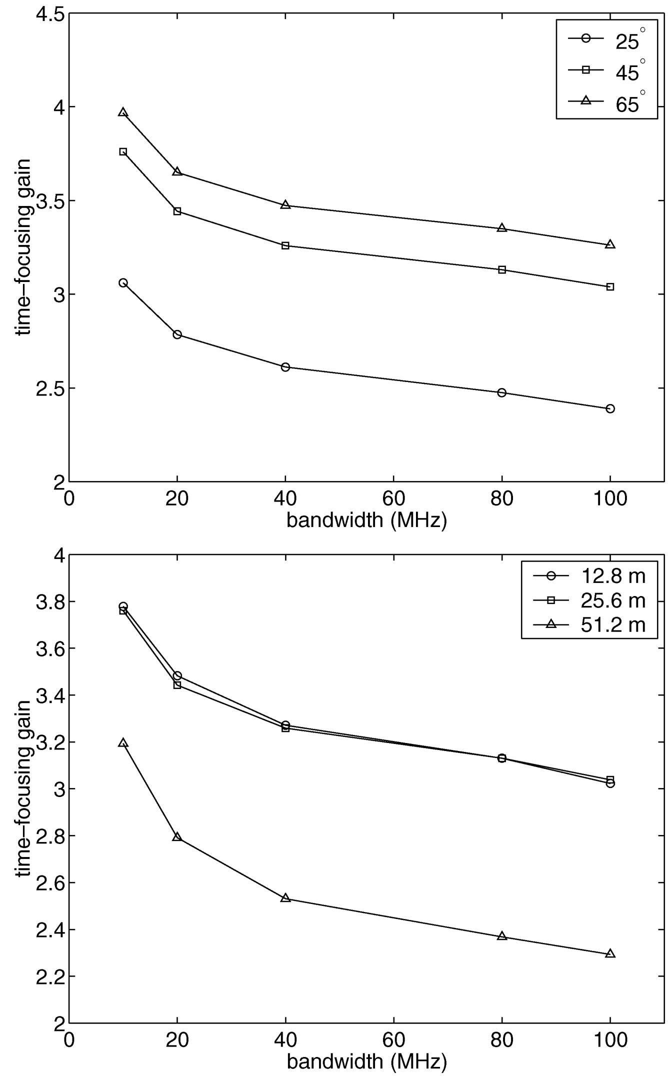


Fig. 11. Asymptotic time-focusing gain (TFG) as a function of bandwidth for different source angles (top) with waveguide width $L_x = 25.6$ m and different waveguide widths (bottom) with source angle $\Delta\vartheta = 45°$.

diversity. From (15) we understand that the number of propagating modes within a fixed angular aperture is set by $\lambda$ and $L_x$. With $\lambda$ fixed and $L_x$ increasing, more propagating modes exists inside the angular aperture. For example, with $\vartheta = 45°$, there are approximately 75, 150, and 301 propagating modes for $L_x = 12.8, 25.6,$ and $51.2$ m, respectively. Time reversal methods exploit this added spatial diversity to tighten the refocusing.

To examine temporal focusing more closely, we show the asymptotic limit of the time-focusing gain in Fig. 11. The top plot is for $L_x = 25.6$ m with different values of $\vartheta$ and the bottom plot is for $\vartheta = 45°$ with different values of $L_x$. All curves decrease monotonically with bandwidth. The main reason for this decrease is that the pulse is narrower as bandwidth increases. The overall delay spread is reduced and the refocus region is not as pronounced. The TFG increases with $\vartheta$ since the additional diversity allows for greater temporal focusing in the sense that ratio between $\Delta\tau$ at and away from $x_0$ becomes greater. Similar to the result for the SFG, we observe that the TFG for $L_x = 12.8$ and 25.6 m are close to each other while the widest waveguide yields a smaller TFG. As $L_x$ increases effects manifested by reflections from waveguide walls decrease and the waveguide domain approaches an unbounded one exhibiting a smaller TFG.

### C. Comparison Between Results Obtained From Both Models

The space-time focusing properties appear in both models. Yet, some differences can be observed. Let us first consider the following similarities:

1) The space-focusing gain increases with bandwidth in both models. In the GS model, it is also shown that the SFG increases similarly with the channel delay-spread. In the waveguide model, simulation results illustrate that the SFG also increases with the channel delay-spread. The increase for the waveguide is related to the source angle and to the inverse of the waveguide width.

2) Space-focusing gain examined using the 3-dB contour shows a weak dependence on bandwidth in both scenarios. Similarly, the dependence on the channel delay-spread is also

weak, but the 3-dB contour decreases as the angle-spread increases. This is clear in the GS model. In the waveguide model, we have observed that the dependence toward the waveguide width is weak, while there is a noticeable dependence on the angle-spread.

Some differences between these two models have been observed. The most pronounced one is that the TFG appears to be independent of the bandwidth in the case of the GS model, while a significant dependence is found in the waveguide. Also, the absolute value of the TFG is much larger in the waveguide scenario. To better understand this difference, we need to refer to the specifics of the models. In the waveguide case, two mechanisms cause delay-spread: large-scale multipath results from the coherent reflections by the waveguide walls, small-scale multipath is caused by the nonhomogeneities of the refractive index. By contrast, the GS propagation only consists of noncoherent reflections, similar to the waveguide small-scale multipathing. Focusing in time reversal is enhanced for bounded domains in that it is more robust. This accounts for the difference seen in these two models. As the waveguide width approaches infinity, it begins to agree with an unbounded medium.

## VI. Conclusion

We have proposed several metrics to characterize space-time focusing resulting from time-reversal methods. We have demonstrated the use of these metrics on two different scattering modes: the geometry-based stochastic model and the random waveguide model. Although these two models have very different mechanisms for multipathing, they yield remarkable similarities in demonstrating the stability of focusing using time-reversal. Therefore, it is believed that time-reversal methods should lead to improved wireless communication systems by highly reliable transmissions and reduced interference to co-channel users.

## References


[1] A. Derode, P. Roux, and M. Fink, "Robust acoustic time reversal with high-order multiple scattering," *Phys. Rev. Lett.*, vol. 75, pp. 4206–4209, 1995.

[2] M. Fink, "Time reversed acoustics," *Phys. Today*, pp. 34–40, March 1997.

[3] ——, "Time-reversed acoustics," *Sci. Amer.*, pp. 91–97, Nov. 1999.

[4] D. R. Dowling and D. R. Jackson, "Phase conjugation in underwater acoustics," *J. Acoust. Soc. Amer.*, vol. 89, pp. 171–181, 1990.

[5] ——, "Narrow-band performance of phase-conjugate arrays in dynamic random media," *J. Acoust. Soc. Amer.*, vol. 91, pp. 3257–3277, 1992.

[6] D. R. Dowling, "Acoustic pulse compression using passive phase-conjugate processing," *J. Acoust. Soc. Amer.*, vol. 95, pp. 1450–1458, 1994.

[7] W. A. Kuperman, W. S. Hodgkiss, H. C. Song, T. Akal, C. Ferla, and D. R. Jackson, "Phase conjugation in the ocean: Experimental demonstration of an acoustic time-reversal mirror," *J. Acoust. Soc. Amer.*, vol. 103, pp. 25–40, 1998.

[8] W. S. Hodgkiss, H. C. Song, W. A. Kuperman, T. Akal, C. Ferla, and D. R. Jackson, "A long-range and variable focus phase-conjugation experiment in shallow water," *J. Acoust. Soc. Amer.*, vol. 105, pp. 1597–1604, 1999.

[9] S. Kim, G. F. Edelmann, W. A. Kuperman, W. S. Hodgkiss, and H. G. Song, "Spatial resolution of time-reversal arrays in shallow water," *J. Acoust. Soc. Amer.*, vol. 110, pp. 820–829, 2001.

[10] D. Rouseff, D. R. Jackson, W. L. J. Fox, C. D. Jones, J. A. Ritcey, and D. R. Dowling, "Underwater acoustic communication by passive-phase conjugation: Theory and experimental results," *IEEE J. Ocean. Eng.*, vol. 26, pp. 821–831, 2001.

[11] M. G. Heinemann, A. Larazza, and K. B. Smith, "Acoustic communications in an enclosure using single-channel time-reversal acoustics," *Appl. Phys. Lett.*, vol. 80, pp. 694–696, 2002.

[12] G. F. Edelmann, T. Akal, W. S. Hodgkiss, S. Kim, W. A. Kuperman, and H. C. Song, "An initial demonstration of underwater acoustic communications using time reversal," *IEEE J. Ocean. Eng.*, vol. 27, pp. 602–609, 2002.

[13] P. Roux, B. Roman, and M. Fink, "Time-reversal in an ultrasonic waveguide," *Appl. Phys. Lett.*, vol. 40, pp. 1811–1813, 1997.

[14] P. Roux and M. Fink, "Time reversal in a waveguide: Study of the temporal and spatial focusing," *J. Acoust. Soc. Amer.*, vol. 107, pp. 2418–2429, 2000.

[15] A. Derode, A. Toupin, J. de Rosny, M. Tanter, S. Yon, and M. Fink, "Taking advantage of multiple scattering to communicate with time-reversal antennas," *Phys. Rev. Lett.*, vol. 90, p. 014 301, 2003.

[16] Y. Chang, H. R. Fetterman, I. L. Newberg, and S. K. Panaretos, "Microwave phase conjugation using antenna arrays," *IEEE Trans. Microwave Theory Tech.*, vol. 46, no. 11, pp. 1910–1919, Sep. 1998.

[17] J. Tuovinen, G. S. Shiroma, W. E. Forsyth, and W. A. Shiroma, "Multipath communications using a phase-conjugate array," in *IEEE MTT-S Int. Microwave Symp. Dig.*, vol. 3, 2003, pp. 1681–1684.

[18] A. Paulraj, R. Nabar, and D. Gore, *Introduction to Space-Time Wireless Communications*. U.K.: Cambridge Univ. Press, 2003.

[19] W. C. Y. Lee, *Mobile Communications Engineering*: McGraw-Hill, 1998.

[20] D. A. McNamara, C. W. I. Pistorius, and J. A. G. Malherbe, *Introduction to the Uniform Theory of Diffraction*. Norwood, MA: Artech House, 1990.

[21] A. Ishimaru, *Wave Propagation and Scattering in Random Media*: Academic Press, 1978, vol. 2.

[22] P. Blomgren, G. Papanicolaou, and H. Zhao, "Super-resolution in time-reversal acoustics," *J. Acoust. Soc. Amer.*, vol. 111, pp. 230–248, 2002.



**Claude Oestges** received the M.S. degree in electrical engineering and the Ph.D. degree in applied science from the Université Catholique de Louvain (U.C.L.), Louvain-la-Neuve, Belgium, in 1996 and 2000, respectively.

In 1997, he spent two months at the Centre for Communication Systems Research, University of Surrey, U.K. He was also involved in the European COST Action 255 "Radiowave Propagation Modeling for New SatCom Services at Ku-band and Above." From January to December 2001, he joined, as a Postdoctoral Scholar, the Smart Antennas Research Group (Information Systems Laboratory), Stanford University, CA. Since September 2001, he has been a Postdoctoral Fellow at the Belgian National Science Foundation – Fonds National de la Recherche Scientifique (FNRS), associated with the Microwave Laboratory, Université Catholique de Louvain (UCL), Louvain-la-Neuve, Belgium. His research interests cover wireless and satellite communications, with a specific focus on propagation. He is currently taking part in the European COST Action 273 "Toward Mobile Broadband Multimedia Networks."

Dr. Oestges received the 1999 and 2000 IEE Marconi Premium Award.

**Arnold D. Kim** received the B.S. degree in engineering science and applied mathematics from Northwestern University, Evanston, IL, in 1995 and the M.S. and Ph.D. degrees in applied mathematics from the University of Washington, Seattle, in 1997 and 2000, respectively.

From August 2001 to June 2004, he was a Postdoctoral Fellow in the Department of Mathematics, Stanford University, Stanford, CA. Since Autumn 2004, he has been an Assistant Professor in the School of Natural Sciences at the University of California, Merced.

**George Papanicolaou** received the Ph.D. degree in mathematics from the Courant Institute of New York University, in 1969.

He joined the faculty of the Courant Institute where he was a Professor from 1976 to 1993. He has been a Professor of mathematics at Stanford University, Stanford, CA, since 1993.

**Arogyaswami J. Paulraj** (F'91) received the Ph.D. degree from the Naval Engineering College and the Indian Institute of Technology, Delhi, India, in 1973.

He has been a Professor with the Department of Electrical Engineering, Stanford University, CA, since 1993, where he supervises the Smart Antennas Research Group. His nonacademic positions included Head, Sonar Division, Naval Oceanic Laboratory, Cochin, India; Director, Center for Artificial Intelligence and Robotics, Bangalore, India; Director, Center for Development of Advanced Computing; Chief Scientist, Bharat Electronics, Bangalore, India; and Chief Technical Officer and Founder, Iospan Wireless Inc., San Jose, CA. He also held visiting appointments at Indian Institute of Technology, Delhi, India; Loughborough University of Technology, Loughborough, U.K.; and Stanford University, CA. He sits at several board of directors and advisory boards for U.S. and Indian companies and venture partnerships. He is the author of over 250 research papers and holds eight patents. His engineering experience includes development of sonar systems, massively parallel computers, and, more recently, broad-band wireless systems. His research has spanned several disciplines, emphasizing estimation theory, sensor signal processing, parallel computer architectures/algorithms, and space-time wireless communications.

Dr. Paulraj is a Member of the Indian National Academy of Engineering. He has won several awards for his engineering and research contributions. These include two President of India Medals, CNS Medal, Jam Medal, Distinguished Service Medal, Most Distinguished Service Medal, VASVIK Medal, IEEE Best Paper Award (joint), among others.